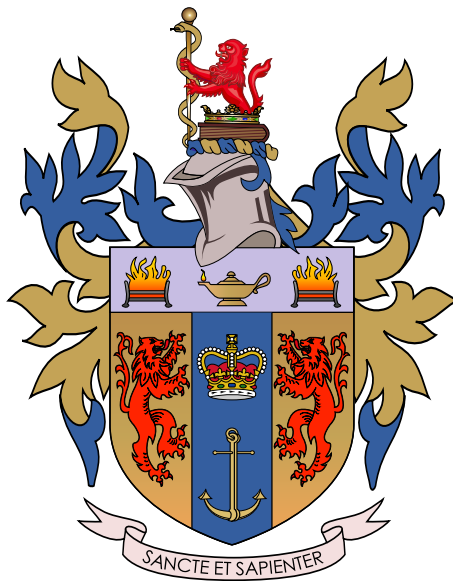


QUANTUM TUNNELLING WITHOUT A BARRIER: PHASE-SENSITIVE SIGNATURES IN HHG

Jude Russell



Supervised by

Dr Emilio Pisanty
Anne Weber

A report submitted in partial fulfillment of requirements for the degree of
Bachelor of Science in Physics

Department of Physics
King's College London
April 2025

Abstract

High harmonic generation (HHG) produces attosecond pulses of light through strong-field interactions between atoms and intense laser fields. A central mechanism in HHG is quantum tunnelling, whereby an electron escapes an atom through a laser-suppressed potential barrier. In this report we investigate the recently predicted mechanism of tunnelling without a barrier, which occurs when the instantaneous electric field vanishes, eliminating the classical barrier altogether. Despite its theoretical significance, an experimental observable for the event remains elusive, and here we examine quantum-path phase coefficients as candidate observables for its identification. These coefficients, which describe the sensitivity of harmonic phase to variations in the driving field, are central to phase matching and coherence in HHG. By mapping their behaviour in a bichromatic field, we find that although no definitive observable emerges, the zero-field tunnelling event shows a strong response in the α_{11} coefficient, indicating potential for detection via phase-sensitive or interference-based techniques.

Contents

Abstract	i
1 Introduction	1
1.1 Attosecond physics	1
1.2 High harmonic generation	1
1.3 Tunnelling without a barrier	2
2 Theory	4
2.1 The strong-field approximation	4
2.2 The saddle point method	7
2.2.1 Picard-Lefschetz theory	8
2.3 Quantum-path phase coefficients	9
3 Results and Analysis	12
3.1 Setup	12
3.2 The monochromatic case	13
3.2.1 The monochromatic harmonic spectrum	13
3.2.2 Phase coefficients for a monochromatic field	14
3.3 The bichromatic case	15
3.3.1 The bichromatic spectrum	15
3.3.2 Zero-field tunnelling phase coefficients	16
3.3.3 Two-colour parameter space	17
3.3.4 Taylor analysis of the phase landscape	19
Discussion	21
Conclusion	23
Bibliography	24

1

Introduction

Contents

1.1	Attosecond physics	1
1.2	High harmonic generation	1
1.3	Tunnelling without a barrier	2

1.1 Attosecond physics

Attosecond physics is the study of ultrafast processes occurring on timescales of 10^{-18} seconds, with the aim to resolve the motion of electrons in atoms, molecules and solids in real time. Enabled by the development of high harmonic generation, the interaction of intense laser fields with matter has made possible the control of electron dynamics on their natural timescales. The scale of an attosecond is difficult to conceptualise. In that time, light will travel about the width of an atom. The orbital period of an electron in a hydrogen atom is around 150 attoseconds. The shortest pulses created to date are on the order ~ 50 attoseconds [1]. Today, attosecond techniques are central to strong-field physics, ultrafast spectroscopy, and the exploration of fundamental quantum processes such as ionisation and tunnelling.

1.2 High harmonic generation

High harmonic generation (HHG) is a highly nonlinear optical process whereby intense laser fields interact with atoms or molecules producing radiation at integer multiples (harmonics q) of the driving laser frequency. HHG is a cornerstone in attosecond science,

enabling the generation of ultrashort pulses of light used to probe electron dynamics in matter at unprecedented time scales.

The physical picture of HHG is best understood through the three-step model [2], which is shown schematically in Fig. 1.1.

1. Tunnel ionisation: An intense laser field focused on an atomic target can distort the potential barrier such that the electron can tunnel out into the continuum.
2. Propagation in the continuum: The free electron is accelerated away by the oscillating laser field, and on reversal of the field driven back towards the ion, gaining kinetic energy.
3. Recombination: The electron can return to its parent ion and recombine with it, releasing its gained kinetic energy as a high-energy photon.

Of these three steps, the first is most conceptually complex. Tunnel ionisation is explained quantum mechanically by some of the electron's wavefunction escaping into the continuum [3]. In this view, the free part of the wavefunction is accelerated by the laser field and returns to the parent ion, interfering with the bound part of the wavefunction. This interference causes the system's dipole moment to oscillate rapidly, resulting in the emission of high-frequency radiation.

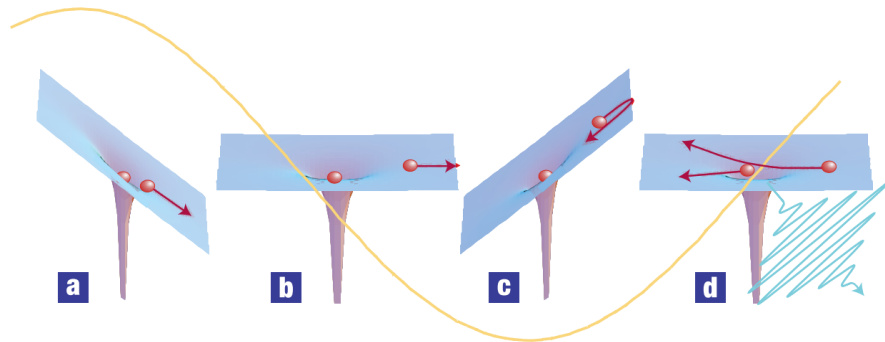


Figure 1.1: Sketch of the three-step model of HHG: tunnel ionisation, propagation in the continuum, and recombination. Figure reproduced from [4].

1.3 Tunnelling without a barrier

In quantum mechanics, tunnelling is the process by which a particle can pass through a potential barrier which would be insurmountable in the classical understanding of physics. This is possible as a result of the wave nature of matter, with each particle having an associated wavefunction which decays exponentially inside a potential barrier, giving it a nonzero probability of being found on the other side. In the context of strong-field

physics, tunnelling occurs when the laser field is strong enough to distort the Coulomb potential of an atom into a barrier through which the electron can escape.

A recent paper [5] discovered a counter-intuitive tunnelling event arising from a bichromatic laser field which occurs when there is no classical barrier. The lack of barrier comes from a two-colour switchover process in the context of strong-field ionisation whereby a laser with frequency ω is gradually replaced by its second harmonic 2ω . At the point in the switchover when the two field components are equal in magnitude, the total electric field has an extremum that reaches zero. This field configuration is shown in black in Fig. 1.2. Tunnel ionisation events occur at all four extrema of the field cycle, including the local minimum where there is no barrier. For this tunnelling without a barrier event, six representative electron trajectories are shown, plotted as their displacement $x(t)$ in atomic units (of Bohr radius) from the ion core. While this particular event does contribute to the harmonic emission, its signal is hidden by the other more dominant orbits [5] with greater ionisation probabilities, in particular the last in the cycle marked in yellow in Fig. 1.2 where the field reaches a global maximum magnitude. This makes direct detection in the energy spectrum difficult, if not impossible.

As a result, a natural goal is to find an observable which can isolate or enhance the unique ionisation event. Since quantum phase influences interference effects in electron trajectories, the aim of the work presented in this report is to find detectable signatures of phase-sensitive observables.

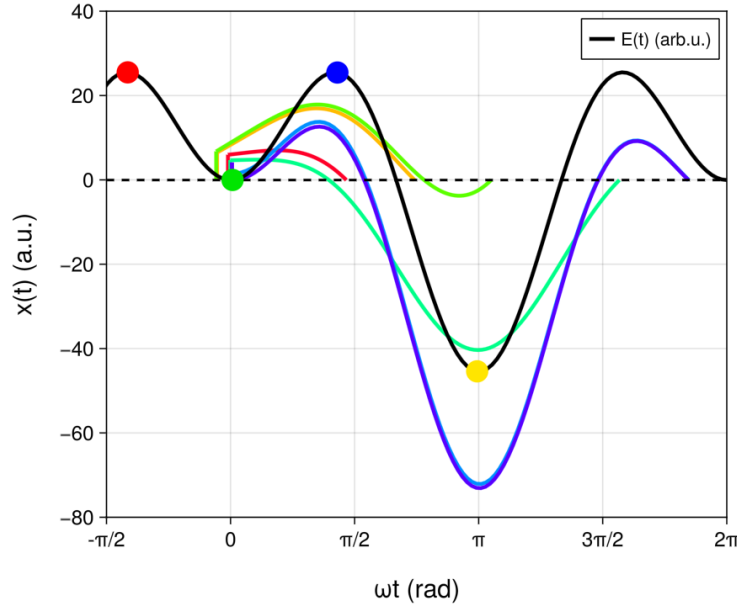


Figure 1.2: Field configuration at the point in the two-colour switchover when each component has equal amplitude (i. e., when $E_1 = E_2$). The total field in black is given by $E(t) = E_1 \cos(\omega t) + E_2 \cos(2\omega t + \phi)$. Each ionisation burst event is marked with a colour, with the zero-field event in green. Six electron trajectories are shown for the second burst.

2

Theory

Contents

2.1	The strong-field approximation	4
2.2	The saddle point method	7
2.2.1	Picard-Lefschetz theory	8
2.3	Quantum-path phase coefficients	9

2.1 The strong-field approximation

We will work under the strong-field approximation (SFA) which models atoms in intense laser fields, as laid out in [3, 6, 7]. The main assumption made is that once the electron is ionised, it is influenced only by the field of the driving laser and that the ion's potential has a negligible effect. The SFA gives qualitative understanding of many strong-field effects and is computationally simpler than numerically solving the time dependent Schrödinger equation. Consider an atom in an intense laser field $\mathbf{E}(t)$. It is described by the Schrödinger equation which takes the form

$$i \frac{d}{dt} |\psi(t)\rangle = \left[\frac{1}{2} \mathbf{p}^2 + V(\mathbf{r}) + \mathbf{r} \cdot \mathbf{E}(t) \right] |\psi(t)\rangle, \quad (2.1)$$

where $|\psi(t)\rangle$ is the electron's time-dependent quantum state, $\mathbf{p} = -i\nabla$ is the momentum operator, and \mathbf{r} is the electron's position. The term $V(\mathbf{r})$ represents the atomic binding potential. The interaction Hamiltonian $\mathbf{r} \cdot \mathbf{E}(t)$ comes from the dipole approximation where we assume that the laser's wavelength is much larger than the atomic size such that the field's spatial variation over the atom is negligible.

Assuming the electron is in its ground state, $e^{-iE_0t} |\psi_0\rangle$, before the laser pulse starts, and that this is the only bound electron state that contributes, we make the ansatz for the wavefunction

$$|\psi(t)\rangle = e^{-iE_0t} |\psi_0\rangle + |\psi_{out}(t)\rangle, \quad (2.2)$$

where $|\psi_{out}(t)\rangle$ is the outgoing continuum electron. Since the SFA ignores the potential of the ion once the electron has left the atom, the outgoing wave equation is the laser-only Schrödinger equation

$$i \frac{d}{dt} |\psi_{out}(t)\rangle = \left[\frac{1}{2} \mathbf{p}^2 + \mathbf{r} \cdot \mathbf{E}(t) \right] |\psi_{out}(t)\rangle. \quad (2.3)$$

This equation can be solved exactly with plane wave solutions. Substituting these solutions into the ansatz (Eq. 2.2) and then substituting this result into the Schrödinger equation simplifies to

$$\begin{aligned} i \frac{\partial a}{\partial t} &= e^{-iE_0t} \langle \Psi_{\mathbf{p}}^{(V)} | \mathbf{r} \cdot \mathbf{E}(t) | \psi_0 \rangle \\ &+ \int d\mathbf{p}' a(\mathbf{p}', t) \langle \Psi_{\mathbf{p}}^{(V)} | V(\mathbf{r}) | \Psi_{\mathbf{p}'}^{(V)} \rangle. \end{aligned} \quad (2.4)$$

Here, the Volkov states $|\Psi_{\mathbf{p}}^{(V)}\rangle$ describe a free electron in the presence of the laser field. In the velocity gauge, they take the form

$$|\Psi_{\mathbf{p}}^{(V)}\rangle = e^{-iS(\mathbf{p}, t)} |\mathbf{p} + \mathbf{A}(t)\rangle, \quad (2.5)$$

where $\mathbf{A}(t)$ is the vector potential of the laser field (with $\mathbf{E}(t) = -\partial_t \mathbf{A}(t)$), and $S(\mathbf{p}, t)$ is the classical action,

$$S(\mathbf{p}, t) = \frac{1}{2} \int d\tau [\mathbf{p} + \mathbf{A}(\tau)]^2. \quad (2.6)$$

The transition amplitude $a(\mathbf{p}, t)$ is the probability amplitude of a transition from the ground state to a state in the continuum with momentum \mathbf{p} . In other words, it is the ionisation probability amplitude. It is given by the projection of the time-evolved wavefunction onto the Volkov states,

$$a(\mathbf{p}, t) = \langle \Psi_{\mathbf{p}}^{(V)} | \psi_{out} \rangle. \quad (2.7)$$

The final approximation is to neglect the second term and solve the remaining ordinary differential equation to obtain a time integral for the transition amplitude

$$a(\mathbf{p}, t) = -i \int_{-\infty}^t dt' \mathbf{E}(t') \cdot \mathbf{d}(\mathbf{p} + \mathbf{A}(t')) \exp \left[-i \int_{t'}^t \left(\frac{1}{2} [\mathbf{p} + \mathbf{A}(\tau)]^2 + I_p \right) d\tau \right] \quad (2.8)$$

where we find the Volkov action in the exponent describing the free electron Volkov states during ionisation and propagation:

$$S_V(\mathbf{p}, t, t') = \int_{t'}^t \left(\frac{1}{2} [\mathbf{p} + \mathbf{A}(\tau)]^2 + I_p \right) d\tau. \quad (2.9)$$

Note that this is not the full classical action which would include the Coulomb interaction; in the SFA we use only the energy part. Here we have introduced the vector potential of the laser field $\mathbf{A}(t)$ and the ionisation potential I_p of the atom.

When the electron recombines in HHG, the harmonic emission comes from the rapid oscillation of the dipole moment given by

$$\mathbf{d}(t) = \int d^3p \mathbf{d}^*(\mathbf{p} + \mathbf{A}(t)) a(\mathbf{p}, t), \quad (2.10)$$

where the dipole matrix element $\mathbf{d}(\mathbf{k}) = \langle \mathbf{k} | \hat{\mathbf{r}} | \psi_0 \rangle$. Here $\mathbf{k}(t) = \mathbf{p} + \mathbf{A}(t)$ is the instantaneous kinematic electron momentum. We can substitute the transition amplitude from before to obtain the Lewenstein integral for the time-dependent dipole moment responsible for the harmonic emission

$$\mathbf{d}(t) = -i \int_{-\infty}^t dt' \int d^3p \mathbf{d}^*(\mathbf{p} + \mathbf{A}(t)) [\mathbf{E}(t') \cdot \mathbf{d}(\mathbf{p} + \mathbf{A}(t'))] e^{-iS_V(\mathbf{p}, t, t')}. \quad (2.11)$$

In order to calculate the harmonic spectrum (the HHG output), we must take the Fourier transform of this time-dependent dipole moment

$$\begin{aligned} \tilde{\mathbf{d}}(q\omega) = & -i \int_{-\infty}^{\infty} dt \int_{-\infty}^t dt' \int d^3p \mathbf{d}^*(\mathbf{p} + \mathbf{A}(t)) [\mathbf{E}(t') \cdot \mathbf{d}(\mathbf{p} + \mathbf{A}(t'))] \\ & \times e^{-iS_V(\mathbf{p}, t, t') + iq\omega t}. \end{aligned} \quad (2.12)$$

This integral can be used to calculate the spectral intensity of the emitted harmonic radiation at frequency $q\omega$ for each harmonic q . We denote frequency-domain dipole moments with a tilde to distinguish them from time-domain quantities. The resulting expression for the harmonic intensity is

$$I(q\omega) \propto (q\omega)^4 \left| \tilde{\mathbf{d}}(q\omega) \right|^2. \quad (2.13)$$

By Fourier transforming the time-dependent dipole, the exponent acquires an additional term. This new phase is the full semiclassical action given by a linear combination of the Volkov action with the energy of the harmonic photon

$$\begin{aligned} S(\mathbf{p}, t, t') &= q\omega t - \int_{t'}^t \left(\frac{1}{2} [\mathbf{p} + \mathbf{A}(\tau)]^2 + I_p \right) d\tau \\ &= q\omega t - S_V(\mathbf{p}, t, t'). \end{aligned} \quad (2.14)$$

The maximum harmonic frequency q_{\max} generated in HHG is identified phenomenologically by the cutoff law

$$q_{\max}\omega \approx I_p + 3.17U_p. \quad (2.15)$$

This relates the cutoff frequency $q_{\max}\omega$ to the target's ionisation potential I_p and the ponderomotive energy $U_p = E^2/4\omega^2$ which is the average kinetic energy gained by the electron as it is oscillated by the field [2, 6]. The SFA predicts a harmonic emission

spectrum from HHG which shows a long plateau region of roughly constant output followed by a sharp drop-off at the harmonic cutoff frequency. This cutoff condition captures the maximum energy an electron can acquire from the field before recombining, and it marks the boundary between efficient harmonic emission and the rapid falloff in signal.

The SFA not only provides a qualitative picture of ionisation and harmonic emission, but also allows us to understand the phase structure of the emitted harmonics through the concept of quantum trajectories. For any given harmonic within the plateau region, there are several electron trajectories whose dipoles contribute to the overall signal. An electron trajectory—or quantum path—is characterised by its ionisation time t' , when the electron tunnels out of the atom, and its recombination time t , when it returns to emit a photon. These are evaluated using the saddle-point approximation, which will be presented in the next section.

For a monochromatic driving laser, the most significant contributions come from stationary points of the exponentiated action, which can be associated with so-called short and long trajectories, distinguished by the time the electron spends in the continuum. These trajectories dominate the harmonic emission spectrum and exhibit distinct phase accumulation behaviours, which depend sensitively on the laser intensity. This sensitivity is captured by the quantum-path phase coefficients, which play a central role in understanding phase matching between the laser and the emission which is crucial for achieving a strong HHG signal by constructive interference.

However, in the bichromatic case we are interested in, where the driving laser field consists of two frequencies ω and 2ω , the situation becomes considerably more complex. The presence of multiple field components breaks the simple symmetry of the monochromatic field, leading to more ionisation bursts within each cycle. As a result, the number of contributing quantum trajectories increases, and their phase relationships become more intricate. The standard classification into “short” and “long” paths becomes inadequate. In such fields, phase-sensitive observables like the quantum-path phase coefficients may provide a potential route for distinguishing subtle processes such as tunnelling without a barrier, where classical intuition no longer applies.

2.2 The saddle point method

The SFA gives us the frequency-dependent dipole moment (Eq. 2.12) of an atom in a strong laser field which is responsible for harmonic emission in HHG. The phase of the exponential in the dipole integral is the semiclassical action (Eq. 2.14) and the exponential’s value oscillates rapidly in time. Such highly oscillatory integrals elude simple direct numerical evaluation, and so they are often approximated using the saddle point method [6, 7]. The rapid oscillation of this phase means that contributions from different points over the domain of the integral tend to cancel each other out. This is only not the case in regions where the phase does not change significantly, and these occur where the phase $S(\mathbf{p}, t, t')$ is stationary. These points dominate the integral’s value

and with the saddle point approximation we can simply calculate them and sum their contributions to find the total dipole moment.

Quantum paths, or orbits taken by electrons in ionisation, propagation and recombination correspond to these saddle points in the action landscape. These are the points in complex time and momentum space at which the action is stationary. To express this compactly, we define a placeholder variable $\tau \in \{\mathbf{p}, t, t'\}$ representing any of the action's dependencies. We must therefore solve the saddle point equation

$$\frac{\partial S(\mathbf{p}, t, t')}{\partial \tau} = 0 \quad (2.16)$$

which yields definitions of the saddle points:

$$\left. \frac{\partial S(\mathbf{p}, t, t')}{\partial t'} \right|_{t'=t_i} = \frac{1}{2} [\mathbf{p} + \mathbf{A}(t_i)]^2 + I_p = 0 \quad (\text{ionisation condition}), \quad (2.17)$$

$$\left. \frac{\partial S(\mathbf{p}, t, t')}{\partial \mathbf{p}} \right|_{\mathbf{p}=\mathbf{p}_s} = \int_{t_i}^{t_r} [\mathbf{p} + \mathbf{A}(t')] dt' = 0 \quad (\text{recollision condition}), \quad (2.18)$$

$$\left. \frac{\partial S(\mathbf{p}, t, t')}{\partial t} \right|_{t=t_r} = \frac{1}{2} [\mathbf{p} + \mathbf{A}(t_r)]^2 + I_p = q\omega \quad (\text{recombination condition}). \quad (2.19)$$

Here we evaluated the derivatives at specified saddle point coordinates which are the ionisation time t_i , the recombination time t_r , and the saddle point momentum \mathbf{p}_s . These saddle points are in general complex numbers. Equation 2.17 describes the tunnelling process, with the ionisation time being the time the electron enters the barrier, and its real part the point at which it exits the barrier. Equation 2.18 states the requirement that the electron returns to its parent ion, and Eq. 2.19 describes the energy conservation involved during its recombination of with atom to produce a photon with energy $q\omega$ where q is the harmonic of the fundamental driving laser frequency [6].

After calculating the saddle points, one is left with a cloud of saddle point solutions which must be classified into distinct quantum paths. While this classification problem is non-trivial, a natural separator between saddle points corresponding to different trajectories arises from the zero points of the second derivative of the semiclassical action [8]. These points, which correspond to the harmonic cutoff times, lie between the saddle points and provide robust markers for classification.

2.2.1 Picard-Lefschetz theory

Not all of the saddle points found with this method contribute to the harmonic emission, and we must determine which solutions are relevant. Many heuristics exist for determining relevant saddle points for trivial field configurations such as in the monochromatic regime, but these fail for more complicated lasers. This is the case for

the two-colour field which produces the tunnelling without a barrier event, and so the standard approach must be extended.

Consider a bichromatic driving laser field with contributing frequencies ω and 2ω of the form

$$E(t) = E_1 \cos(\omega t) + E_2 \cos(2\omega t + \phi) \quad (2.20)$$

with the electric field amplitudes E_1 and E_2 and a phase shift ϕ . In the case of these fields there are many saddle points and so we require a rigorous approach to determine which of them is relevant to the HHG process. To do this we will apply Picard-Lefschetz theory. This framework, as will be laid out in [9], applies a deformation to the integration path of the dipole integral (Eq. 2.12) from the SFA. In particular, the integral path—the domain along which the integral is evaluated—is deformed to a new integration contour in the complex plane called a Lefschetz thimble. This thimble is the path along which the integrand oscillates the least and decays most rapidly. Each thimble is associated to a saddle point and represents the contour of steepest descent. The integrand's magnitude is determined by the real part of the exponent $h(t_i, t_r) = \text{Re}[S/\hbar]$, so in the case of the dipole integral, thimbles are the contours of steepest descent of the real part of the action. This contour is defined by

$$\frac{dx_i}{d\lambda} = - \left(\frac{\partial h}{\partial x_i} \right)^*, \quad x_i \in t_i, t_r, \quad (2.21)$$

where λ is the flow parameter for how far the original integration contour has been deformed and $(\cdot)^*$ denotes the complex conjugate. This contour converges to contain the saddle points which we wish to check for contribution to the integral. A saddle point is deemed relevant if its dual thimble crosses the original integration domain. The dual thimble is the contour of steepest *ascent* and is defined in analogy to the thimble as

$$\frac{dx_i}{d\lambda} = + \left(\frac{\partial h}{\partial x_i} \right)^*, \quad x_i \in t_i, t_r. \quad (2.22)$$

Since the original integration domain is the space of real times (in \mathbb{R}^2), we can determine whether a saddle point contributes from its intersection number n_σ

$$n_\sigma = \langle K_\sigma, \mathbb{R}^2 \rangle \quad (2.23)$$

where K_σ is the dual thimble. The intersection number is an integer which counts the intersections between the dual thimble and the original integration domain and relevant saddle points are those for which $n_\sigma \neq 0$.

2.3 Quantum-path phase coefficients

The quantum phase ϕ associated with each electron trajectory originates from the complex-valued semiclassical action $S(t, t')$, where t' is the ionisation time and t the recombination time, obtained via the saddle-point approximation of the transition

amplitude. Because the full action is complex, with the imaginary part encoding tunnelling probability amplitude and wavepacket attenuation, the physically-relevant phase for coherent emission corresponds to the real part of the action. Therefore the essential phase information is approximated by the real part of the semiclassical action

$$\phi = \text{Re}[S(t, t')]. \quad (2.24)$$

Note that in the previous section we called this quantity h , but from now on it will be referred to as ϕ . Each trajectory has an associated dipole moment $\tilde{\mathbf{d}}_s(q\omega)$ which can be summed over all trajectories to give the total dipole $\tilde{\mathbf{d}}(q\omega) = \sum \tilde{\mathbf{d}}_s(q\omega)$. We assume each $\tilde{\mathbf{d}}_s(q\omega)$ has a phase proportional to the driving laser intensity $I = E^2/2$:

$$\tilde{\mathbf{d}}_s(q\omega) \approx e^{-i\alpha I} \quad (2.25)$$

Here α is the quantum-path phase coefficient which characterises the sensitivity of the phase to the laser intensity. It is dependent on the particular trajectory and the harmonic of the emitted photon. This approximation is motivated by the fact that the phase ϕ is intensity dependent. We can therefore expand linearly around some intensity I_0 [10]:

$$\phi(I) \approx \phi(I_0) + \left. \frac{\partial \phi}{\partial I} \right|_{I=I_0} \cdot (I - I_0). \quad (2.26)$$

Denoting $\alpha = \left. \frac{\partial \phi}{\partial I} \right|_{I=I_0}$ and absorbing the constants, we have

$$\phi(I) \approx \phi(0) + \alpha I \implies e^{i\phi(I)} \approx e^{i\phi(0)} e^{i\alpha(I)}. \quad (2.27)$$

In a two-colour field, the total intensity is formed of two electric field components E_1 and E_2 with frequencies ω and 2ω . Since the intensity depends on these components non-linearly, ϕ is a function of E_1 and E_2 . In order to capture the second-order sensitivity of the phase to these components, we write the quantum-path phase coefficient matrix α as the Hessian of the phase with respect to E_1 and E_2 .

$$\alpha = \begin{bmatrix} \frac{\partial^2 \phi}{\partial E_1^2} & \frac{\partial^2 \phi}{\partial E_1 \partial E_2} \\ \frac{\partial^2 \phi}{\partial E_2 \partial E_1} & \frac{\partial^2 \phi}{\partial E_2^2} \end{bmatrix} \quad (2.28)$$

The phase can be approximated with a Taylor expansion, which is useful for determining which terms (linear, quadratic, etc.) are dominant in the phase sensitivity to the field.

$$\begin{aligned} \phi(E_1, E_2) \approx & \phi_0 + \frac{\partial \phi}{\partial E_1} \Delta E_1 + \frac{\partial \phi}{\partial E_2} \Delta E_2 \\ & + \frac{1}{2} \left(\frac{\partial^2 \phi}{\partial E_1^2} \Delta E_1^2 + 2 \frac{\partial^2 \phi}{\partial E_1 \partial E_2} \Delta E_1 \Delta E_2 + \frac{\partial^2 \phi}{\partial E_2^2} \Delta E_2^2 \right) \end{aligned} \quad (2.29)$$

Here $\Delta E_i = E_i - E_i^0$ and the derivatives are to be evaluated at the expansion point. In order to approximate the derivatives, the central difference approximation can be used. This method uses the function's value at points equidistant from the point at which the derivative is to be calculated.

3

Results and Analysis

Contents

3.1	Setup	12
3.2	The monochromatic case	13
3.2.1	The monochromatic harmonic spectrum	13
3.2.2	Phase coefficients for a monochromatic field	14
3.3	The bichromatic case	15
3.3.1	The bichromatic spectrum	15
3.3.2	Zero-field tunnelling phase coefficients	16
3.3.3	Two-colour parameter space	17
3.3.4	Taylor analysis of the phase landscape	19

3.1 Setup

The results presented in the following sections were obtained using certain fixed parameters. In all cases, the atomic target was argon gas with an ionisation potential of 15.7596 eV. For the monochromatic calculations, a laser wavelength of 800 nm was used. In the bichromatic cases, the configuration involved a switchover from 800 nm to 400 nm radiation.

The calculations presented in this report were performed using a codebase developed by the Attosecond Physics Group at King's College London, available internally at [11]. Access to this repository is restricted to staff and students of King's College London. The codebase provides the framework for solving the saddle-point equations and analysing quantum trajectories in strong-field ionisation. The implementation of the

tunnelling-without-barrier model, as well as the numerical evaluation and interpretation of the resulting trajectories presented in this report, are original contributions of the author.

3.2 The monochromatic case

3.2.1 The monochromatic harmonic spectrum

The standard setup for a HHG process driven by a monochromatic laser field serves as the basis for understanding quantum-path dynamics. Figure 3.1 shows the characteristic harmonic spectrum generated by a driving laser with a peak intensity of $4 \times 10^{14} \text{ W cm}^{-2}$. The features predicted by the three-step model are clearly visible: a long plateau region associated with high-energy electron recollisions, followed by a sharp cutoff at around the 63rd harmonic.

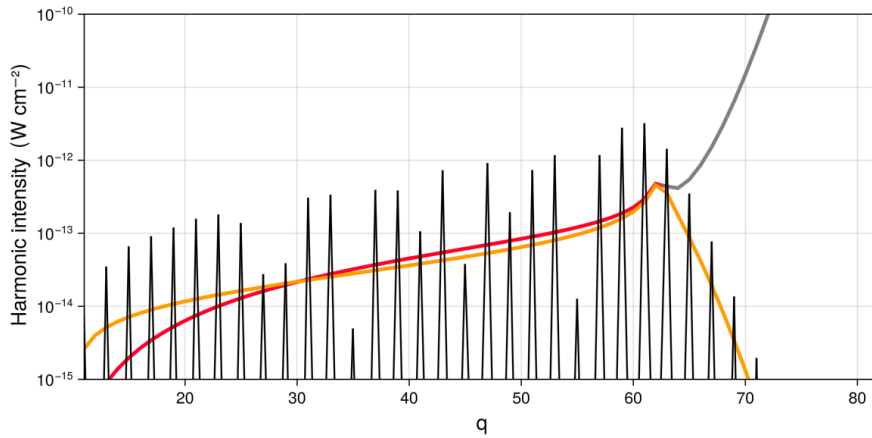


Figure 3.1: The harmonic spectrum for monochromatic HHG. After the cutoff, the long trajectory is not relevant (grey). The total intensity is shown in black.

Each contributing trajectory corresponds to a quantum path where an electron is ionised, accelerated away from and back to the ion, recombining with it and releasing a photon. The plateau reflects the regime where multiple electron trajectories with sufficient energy interfere constructively, whereas the sharp cutoff corresponds to the classical energy limit for recombination. These trajectories were identified as saddle point solutions which were computed by locating stationary points of the action in the complex time plane. Physically, each saddle point corresponds to a path for which the phase of the dipole moment is stationary, leading to constructive interference in the harmonic spectrum. This approach is in the spirit of Feynman's path integral formalism, where the quantum amplitude is obtained by summing over all possible paths, with dominant contributions arising from those with stationary action.

To determine which saddle points contribute physically to the HHG process, we apply the formal framework of Picard-Lefschetz theory, which provides a mathematically rigorous method for assessing which saddle points are relevant in oscillatory integrals like the Lewenstein integral (Eq. 2.11). In this context, a saddle point (t', t) of the semiclassical action $S(\mathbf{p}, t', t)$ is relevant to the HHG signal if and only if its associated steepest-ascent contour known as its “dual thimble”, given by Eq. 2.22, intersects the original real-valued integration domain (\mathbb{R}^2). This method is explained in greater detail in section 2.2.1. The intersection between the deformed and original domains ensures that the saddle point contributes to the total dipole integral.

Only contributing saddle points—those associated with real harmonic emission—were retained and are shown in colour; unstable or divergent trajectories, which do not contribute significantly to the harmonic signal and which return a value of zero in Eq. 2.23, are coloured grey. Here we show the first two returns, one short and one long trajectory, with the long trajectory in red becoming irrelevant after the cutoff due to it having insufficient return energy to meet the recombination condition (see Eq. 2.19). The interference between these trajectories determines the total intensity of the emitted harmonics q and due to the symmetry of the oscillating laser field, the odd-harmonics cancel out. This is what leads to the characteristic structure of the spectrum in such symmetric driving fields, where only even harmonics remain. It is important to note that these interference effects are only visible due to the coherent summation of the dipoles before their total intensity is calculated.

3.2.2 Phase coefficients for a monochromatic field

Since the phase accumulated along a trajectory depends sensitively on the laser intensity, the intensity dependence of the quantum-path phase coefficient α serves as a direct probe of the phase matching behaviour of the emitted harmonics. Phase matching between the driving laser field and the generated harmonic is critical for achieving constructive interference and a strong output signal. Thus an intensity scan was performed to trace the evolution of α .

The phase coefficient α was determined by numerically evaluating the derivative of the real part of the semiclassical action $S(t, t')$ at the saddle point times with respect to the laser intensity (see Eq. 2.16). The resulting values are plotted in Fig. 3.2, which shows the intensity-dependent behaviour of α for the short and long trajectories contributing to a fixed harmonic order of $q = 25$. The laser intensity ranges from 0.5 to $3 \times 10^{14} \text{ W cm}^{-2}$.

The short trajectory in orange consistently exhibits a weaker phase sensitivity (lower α) due to its shorter excursion time in the continuum. In contrast, the long trajectory accumulates a greater phase with increasing intensity, resulting in a stronger intensity dependence of that trajectory’s phase. These two quantum paths dominate the harmonic emission as higher-order terms involving longer excursion times either did not meet the high energy recombination condition or had excessive phase variation which prevented significant coherence. The trajectories coalesce at the harmonic cutoff, beyond which no

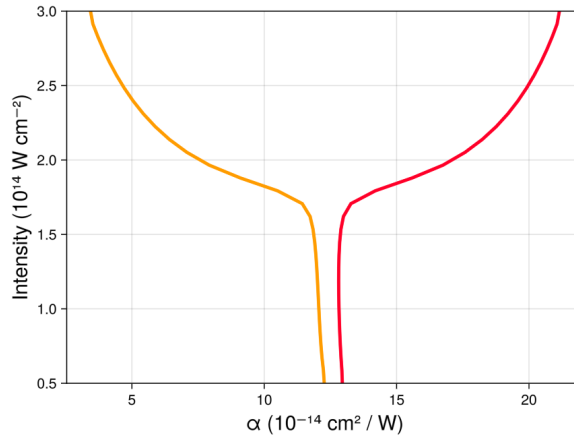


Figure 3.2: Phase coefficient α for the short (orange) and long (red) trajectories contributing to harmonic order $q = 25$. The short trajectory shows weaker intensity dependence due to its shorter excursion time, while the long trajectory exhibits stronger phase sensitivity.

real solution exists for the longer return path. This transition is reflected in the divergent α curves meeting below an intensity threshold.

3.3 The bichromatic case

3.3.1 The bichromatic spectrum

Now we will consider how the harmonic emission spectrum is different during the process of a colour switchover from a monochromatic driver to its second harmonic. Figure 3.3 depicts the harmonic spectrum for a two-colour laser configuration with equal field components (halfway through the switchover) and a peak intensity of $4 \times 10^{14} \text{ W cm}^{-2}$. This is the configuration (see Fig. 1.2) that gives rise to the zero-field tunnelling event. We assume six electron trajectories per ionisation burst, with a distinct colour assigned to every trajectory within a burst. The classification of the calculated saddle points into distinct trajectories is performed by finding the zero points of the second derivatives of the action which sit between the saddle point solutions [8]. The trajectories are coloured according to their classifications with the total spectrum calculated by a coherent summation of the dipole moments shown in black.

Compared to the monochromatic case, introducing a bichromatic driving field significantly increases the complexity of the harmonic spectrum. This complexity arises due to interference effects between multiple quantum paths as they come close in energy. This can boost the intensity of some harmonic frequencies; a feature that can be intentionally tuned to optimise attosecond pulse generation [12, 13]. The more complicated interference also leads to a harmonic cutoff which is not as sharp as in the

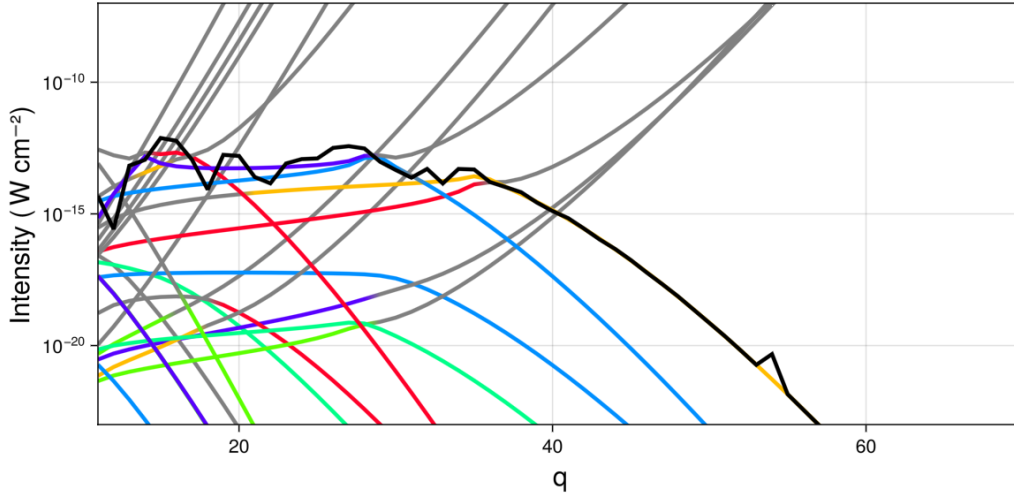


Figure 3.3: Harmonic spectrum for a bichromatic field with equal components with a peak intensity of $4 \times 10^{14} \text{ W cm}^{-2}$. Trajectories are colour-classified with the total spectrum in black and physically irrelevant paths in grey.

monochromatic case shown in Fig. 3.1. Instead, the total spectrum shows multiple dips and peaks along the plateau which continue into the cutoff. This complex scenario sits between two more easily explained cases which are the monochromatic fully ω and fully 2ω configurations, and the interfering trajectories impact the phase structure of the generated harmonics. The harmonic spectrum alone offers limited insight into the subdominant tunnelling without a barrier event. As such, we must turn to more nuanced phase-based observables in an attempt to isolate its contributions.

3.3.2 Zero-field tunnelling phase coefficients

While quantum-path phase coefficients have been studied in the monochromatic case [10], their behaviour in bichromatic fields, particularly in configurations involving a two-colour switchover, has not been explored. The following analysis provides a detailed numerical study of α in this regime, with particular attention to features associated with the tunnelling without a barrier (TWOB) event.

Quantum-path phase coefficients α were determined by the numerical differentiation of the real part of the semiclassical action with respect to the driving laser field intensity. Figure 3.4 depicts an intensity scan of $\alpha(I)$ for the 40th harmonic over an intensity range of 0.2 to $4 \times 10^{14} \text{ W cm}^{-2}$. In Fig. 3.4a, the coefficients for trajectories from all four ionisation events within the cycle are shown, and in Fig. 3.4b, the trajectories from the zero-field tunnelling event are isolated. Each trajectory is coloured according to its classification using the method described previously.

The scan shows quantum orbits forming phase coefficients which take part in multiple

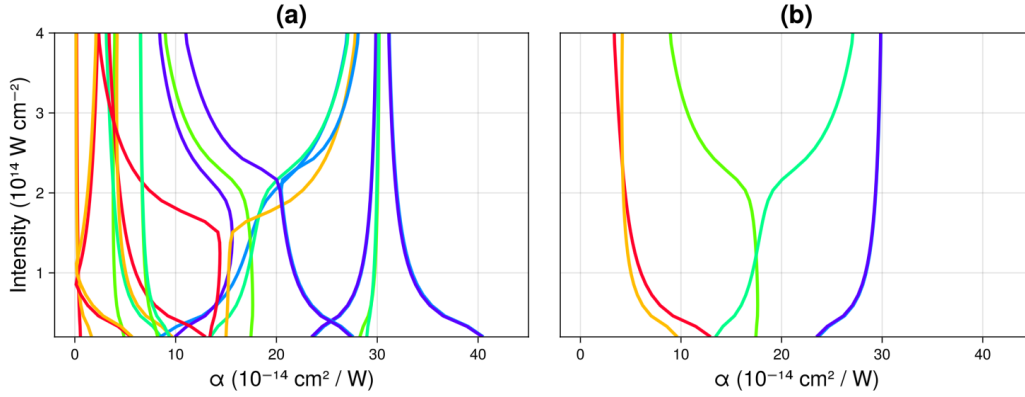


Figure 3.4: Intensity-dependent quantum-path phase coefficients α for the 40th harmonic for (a) all trajectories from the full laser cycle and (b) trajectories contributing to the second ionisation event (tunnelling without a barrier).

partial coalescences and cutoffs. As a result of the asymmetric field and the modified recombination times, many more saddle point trajectories contribute to the emission, and these trajectories do not follow the clean “short” and “long” classifications seen in the monochromatic case. The calculated phase coefficients α display multiple branchings, crossings, and cutoffs across the intensity scan. Many of these features correspond to partial coalescences between trajectories or to the termination of a given trajectory when the harmonic cutoff is reached.

One of the main differences between monochromatic and bichromatic HHG is the appearance of partial coalescences—points where two or more quantum trajectories come very close together before separating again. In the monochromatic case, there was just one clear coalescence near the harmonic cutoff, where the short and long trajectories merge. However, in a bichromatic field, the more complex shape of the driving laser causes several of these near-merging events to occur, making the overall phase behaviour more complicated.

This is evident in Fig. 3.4, where the intensity dependence of the phase coefficient $\alpha(I)$ shows different trajectories moving closer together or further apart, causing noticeable changes in the gradient or shape of the $\alpha(I)$ curves. These features are a direct result of the extra interference between trajectories in the bichromatic field.

3.3.3 Two-colour parameter space

To further understand the phase sensitivity of the high harmonic emission near the tunnelling without a barrier configuration, we analysed the phase coefficient in the vicinity of equal field components $E_1 = E_2$. To investigate the influence of the two-colour electric field components on the quantum-path phase, we numerically evaluated the second derivatives of the real part of the semiclassical action across intensity scans for the individual field components. These values correspond to varying the amplitudes of

two laser fields with different frequencies, forming a bichromatic driving field.

With the addition of this second field component, the quantum-path phase coefficient takes values over two dimensions. Furthermore, the coefficient now has contributions from four of its second derivatives with respect to the field components E_1 and E_2 . These derivatives naturally form a matrix and we will label its elements α_{11} and α_{22} for the diagonal elements, and α_{12} and α_{21} for the cross terms (which are equivalent in our case). The matrix α is depicted in Eq. 3.1.

$$\alpha = \begin{bmatrix} \alpha_{11} & \alpha_{12} \\ \alpha_{21} & \alpha_{22} \end{bmatrix} = \begin{bmatrix} \frac{\partial^2 \phi}{\partial E_1^2} & \frac{\partial^2 \phi}{\partial E_1 \partial E_2} \\ \frac{\partial^2 \phi}{\partial E_2 \partial E_1} & \frac{\partial^2 \phi}{\partial E_2^2} \end{bmatrix} \quad (3.1)$$

By exploring a grid centred around equal intensities (the tunnelling without a barrier setup), we aim to map the sensitivity of the quantum-path phase coefficient to slight asymmetries or imbalances in the field configuration. In order for experimental detection to be viable, our observable must be notably distinct in comparison to the other ionisation events which occur around it, and have a stronger contribution to the spectrum. The aim is to resolve regions where TWOB contributions become significant and yield a phase behaviour distinguishable from the surrounding, more conventional ionisation events.

Figure 3.5 presents the surfaces formed by the values these matrix elements take across an electric field range of 0.06-0.085 atomic units (a.u.). The top row shows the second derivatives of the real part of the action, and the bottom row shows the second derivatives of the imaginary part of the action. One of the cross terms has been omitted as they were found to be equivalent. The phase coefficients are those which come from the real part of the action as this is what corresponds to the accumulation of phase by quantum orbits as they propagate. This accumulation influences the interference of the emission as well as the harmonic cutoff energy, and so it is these coefficients which are crucial in experimental detection. The imaginary part of the action, on the other hand, relates to the attenuation of ionisation probability [8], and these derivatives are shown for completeness.

Each surface represents one of the four ionisation bursts within a single cycle of the bichromatic laser field, with the bursts distinguished by colour. The first and third ionisation events (shown in red and blue) contribute equally to the harmonic spectrum, while the dominant burst is the fourth (in yellow). The tunnelling without a barrier event, the second ionisation burst, has its corresponding phase coefficient surface shown in green. It is this ionisation event whose experimental detection is of significant interest.

The matrix element for which the second ionisation burst has the strongest phase sensitivity is the first, α_{11} , calculated from the real part of the action. For all other elements, the TWOB surface either sits within those of the other events, or has a weaker phase sensitivity than other events (as in Figs. 3.5b and 3.5c). The α_{11} coefficients remains the strongest for the TWOB event across all emitted harmonics.

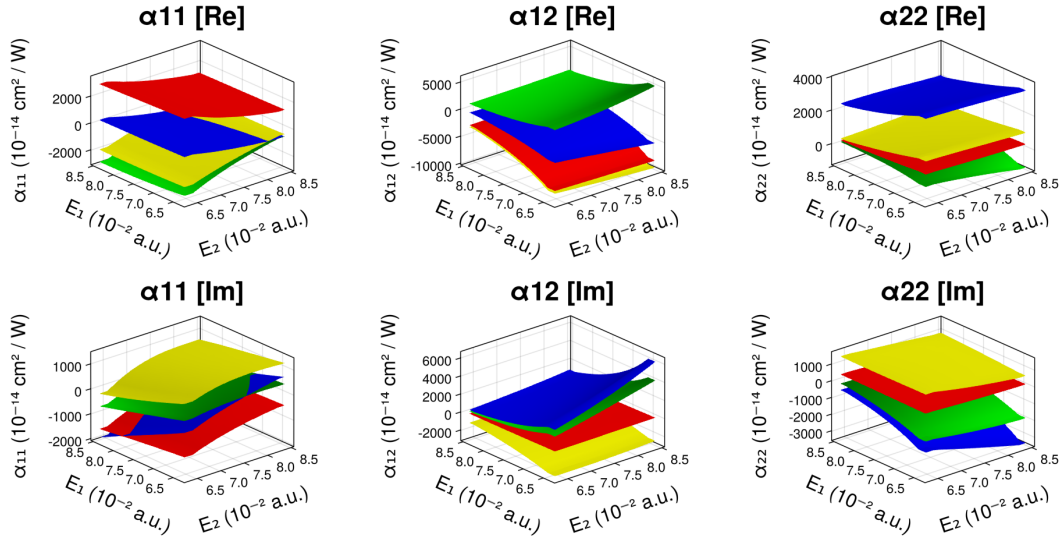


Figure 3.5: Surfaces of the elements in the quantum-path phase coefficient matrix for the fourth return trajectory for each of the four ionisation bursts in one cycle for a strongly bichromatic driving laser field. The tunnelling without a barrier event is shown in green. The top row is calculated as the second derivative of the real part of the action and the bottom row is for the same calculation with the imaginary part.

3.3.4 Taylor analysis of the phase landscape

To quantify the order of dependence and structure of the phase coefficient surfaces discussed in the previous section, we performed a Taylor expansion of the phase $\phi(E_1, E_2)$ around a reference point (E_1^0, E_2^0) . Using Eq. 2.29, the dipole phase given by the real part of the semiclassical action $S(t, t')$ can be approximated to second order using derivatives with respect to the electric field components of the two-colour laser field.

Analysis of this expansion reveals distinct phase dependence for the second (TWOB) and fourth (dominant) ionisation bursts. Figure 3.6 compares the reconstructed phase surfaces from the Taylor expansion with direct numerical evaluations of $\phi(E_1, E_2)$, highlighting key differences in their sensitivity to field variations. The particular trajectories analysed here are the fourth electron returns in the second and fourth ionisation bursts over a grid of electric field values spanning 0.06 to 0.085 a.u. for the 25th harmonic.

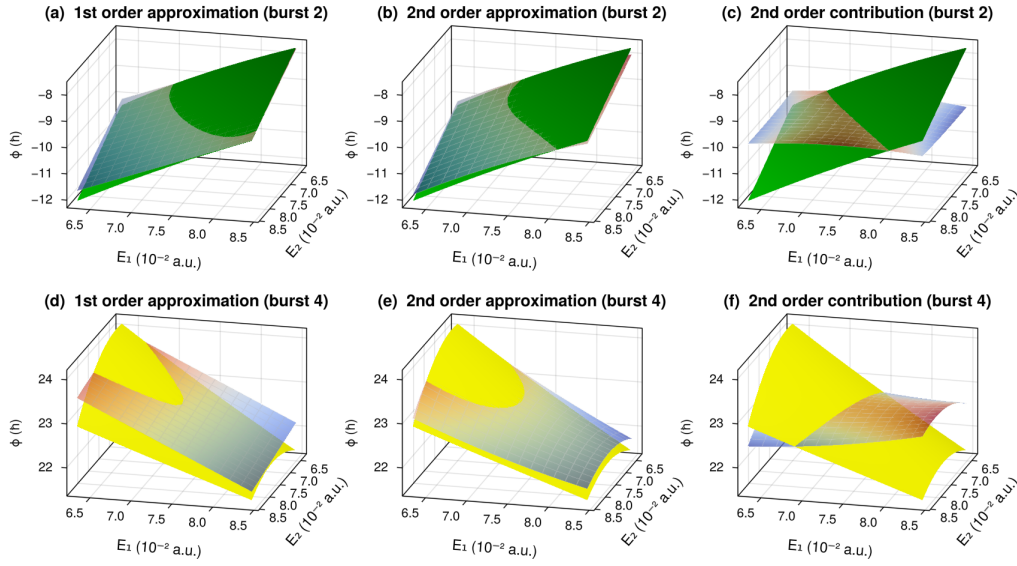


Figure 3.6: Taylor series approximations of the real part of the semiclassical action compared with its computed surfaces for the second ionisation burst (TWOB, top row) and the fourth burst (bottom row) over a scan of independent E_1 and E_2 . Computed surfaces are in solid green and yellow, while the approximation surfaces are semi-transparent. The first-order approximations (a, d) are compared with the second-order approximations (b, e) and the pure second-order contributions (c, f).

For the second burst (TWOB, top row), the first-order (linear) terms dominate the phase variation, capturing the principal intensity dependence. The second-order corrections represented by the Hessian matrix (see Eq. 3.1) introduce subtle curvature, but remain subdominant overall. This suggests that the TWOB phase response is predominantly linear for most trajectories. Across most of the domain, the discrepancy between the full calculation and the second-order expansion remains minimal, indicating that the first-order Taylor expansion accurately captures the essential structure of the phase landscape.

In contrast, the fourth burst (bottom row) displays pronounced curvature, with the first-order approximation failing to capture the full structure. Here, the second-order terms significantly improve the agreement. This indicates that the dominant burst's phase landscape is more complex, requiring higher-order analysis for accurate reconstruction.

Across both bursts, the discrepancy between the full calculation and the second-order expansion remains minimal for moderate field strengths, confirming the Taylor expansion's utility in mapping the phase landscape. Furthermore, the TWOB event's distinguishable α_{11} sensitivity highlights its potential as a probe for zero-field tunnelling dynamics.

Discussion

The work presented in this report set out to explore whether the quantum-path phase coefficients could be used as a diagnostic tool for detecting the unique zero-field tunnelling event predicted in bichromatic HHG by a previous study [5]. Through a detailed theoretical and numerical analysis rooted in the strong-field approximation and saddle point methods, this report investigated the behaviour of quantum trajectories under both monochromatic and bichromatic laser fields.

The focus of the investigation was the quantum path phase coefficient α , a parameter that captures the intensity-dependent phase variation of harmonic emission along different electron trajectories. This coefficient plays a key experimental role, as it governs the spatiotemporal structure of the harmonic radiation—affecting both the divergence of the beam and the chirp or spectral broadening of the emitted light [14, 15]. These effects enable the spatial and temporal separation of quantum path contributions, making α a promising candidate for probing underlying electron dynamics.

In the monochromatic case, the results aligned well with established theory. The harmonic spectrum exhibited a characteristic plateau with a sharp cutoff, and the calculated quantum-path phase coefficients displayed well defined distinctions between the short and long trajectories. As expected, the long trajectory showed greater sensitivity to laser intensity, as a result of its greater phase accumulation during electron excursion.

Looking at the bichromatic field configuration critical to studying tunnelling without a barrier, the phase dependence became notably more complex. The introduction of a second frequency component and a gradual continuous switch to that frequency creates a configuration in which the electric field instantaneously reaches zero, allowing for a non-classical ionisation event in the absence of a traditional potential barrier. This scenario introduced a greater number of relevant quantum trajectories and led to overlapping and coalescing phase structures. The presence of multiple partial coalescences and ill-defined harmonic cutoffs reflects the more chaotic and less symmetric phase dynamics introduced by the bichromatic field.

Detection of the TWOB event provides an experimental challenge due to its subdominant signal in the spectrum, however, this phase dependence analysis provided some promising features. The second derivative surfaces of the semiclassical action revealed that, among the four ionisation bursts per field cycle, the TWOB event exhibits a strong response in the α_{11} phase coefficient. Additionally, Taylor analysis of the dipole phase revealed that for the TWOB event, the phase response was primarily linear in the laser field parameters, unlike the more curved, higher-order behaviour seen in the dominant ionisation burst. The TWOB event might be accessible through interference-based observables, such as spatial or spectral ring structures in far-field interference patterns.

While showing some promise, the quantum-path phase coefficients examined in this report do not on their own provide a clear experimental signature that would allow for isolation or measurement of the TWOB event. Instead, they lay the groundwork for identifying where phase related signatures might emerge and suggest possible criteria for the future development of such an observable.

Conclusion

This report explored the feasibility of using quantum-path phase coefficients to detect the theoretically predicted mechanism of tunnelling without a barrier in high harmonic generation driven by a strongly bichromatic field. The results confirmed that this regime produces a more complex phase structure than the traditional monochromatic case, with significant mixing of quantum trajectories and increased sensitivity to the field configuration.

While no single phase coefficient emerged as a definitive observable for the TWOB event, the α_{11} component of the phase coefficient matrix showed enhanced sensitivity for the TWOB trajectory. Moreover, the dominant linear behaviour in the phase dependence of TWOB trajectories suggests that further analysis of how the field affects interference could reveal observable signatures. One potential future avenue is to study spectral or spatial interference patterns which may arise from the coherent overlap of different trajectories.

Importantly, this work presents the first calculation of quantum-path phase coefficients in a bichromatic HHG field, specifically in the context of tunnelling without a barrier and makes a contribution to the theoretical understanding of strong-field ionisation dynamics. Open questions remain regarding how best to isolate the TWOB signal from competing ionisation bursts in a practical experimental setting. Further work could involve simulating the full spatiotemporal HHG output and identifying any signatures in the diffraction pattern.

In conclusion, while this project did not uncover a definitive observable for tunnelling without a barrier, it identified promising directions for future research and highlighted the utility of phase coefficient analysis as a sensitive probe of quantum dynamics in strong-field ionisation. The results provide both theoretical insight and practical foundations for subsequent investigations into this novel and counterintuitive tunnelling process.

Bibliography

- [1] T. Gaumnitz et al., “Streaking of 43-attosecond soft-x-ray pulses generated by a passively cep-stable mid-infrared driver,” *Opt. Express* **25**, 27506–27516 (2017).
- [2] P. B. Corkum, “Plasma perspective on strong field multiphoton ionization,” *Phys. Rev. Lett.* **71**, 1994 (1993).
- [3] E. Pisanty Alatorre, “Electron dynamics in complex time and complex space,” PhD thesis (Imperial College London, Sept. 2016).
- [4] P. B. Corkum and F. Krausz, “Attosecond science,” *Nature Physics* **3**, 381 (2007).
- [5] A. Weber, M. Khokhlova, and E. Pisanty, “Quantum tunneling without a barrier,” *Phys. Rev. A* **111**, 043103 (2025).
- [6] M. Lewenstein et al., “Theory of high-harmonic generation by low-frequency laser fields,” *Phys. Rev. A* **49**, 2117 (1994).
- [7] O. Smirnova and M. Ivanov, “Multielectron high harmonic generation: simple man on a complex plane,” in *Attosecond and xuv physics* (2014), pp. 165–193.
- [8] E. Pisanty, M. F. Ciappina, and M. Lewenstein, “The imaginary part of the high-harmonic cutoff,” *Journal of Physics: Photonics* **2**, 034006 (2020).
- [9] A. Weber et al., *In preparation*, 2025.
- [10] V. E. Nefedova et al., “Determination of the spectral variation origin in high-order harmonic generation in noble gases,” *Phys. Rev. A* **98**, 033414 (2018).
- [11] Atto Group at King’s College London, *Tunnelling without barrier codebase*, <https://github.kcl.ac.uk/Atto-King-s/Tunnelling-without-barrier>, Access limited to KCL staff and students, 2023.
- [12] O. Raz et al., “Spectral caustics in attosecond science,” *Nature Photonics* **6**, 170–173 (2012).
- [13] A.-K. Raab et al., *Nanophotonics*, 1191–1196 (2025).
- [14] F. Catoire et al., “Complex structure of spatially resolved high-order-harmonic spectra,” *Phys. Rev. A* **94**, 063401 (2016).
- [15] M. B. Gaarde et al., “Spatiotemporal separation of high harmonic radiation into two quantum path components,” *Phys. Rev. A* **59**, 1367–1373 (1999).